Trajectory Smoothing Using GNSS/PDR Integration Via Factor Graph Optimization in Urban Canyons

Yihan Zhong, Weisong Wen*, and Li-Ta Hsu

Abstract—**Accurate and smooth global navigation satellite system (GNSS) positioning for pedestrians in urban canyons is still a challenge due to the multipath effects and the non-light-of-sight (NLOS) receptions caused by the reflections from surrounding buildings. The recently developed factor graph optimization (FGO) based GNSS positioning method opened a new window for improving urban GNSS positioning by effectively exploiting the measurement redundancy from the historical information to resist the outlier measurements. Unfortunately, the FGO-based GNSS standalone positioning is still challenged in highly urbanized areas. As an extension of the previous FGO-based GNSS positioning method, this paper exploits the potential of the pedestrian dead reckoning (PDR) model in FGO to improve the GNSS standalone positioning performance in urban canyons. Specifically, the relative motion of the pedestrian is estimated based on the raw acceleration measurements from the onboard smartphone inertial measurement unit (IMU) via the PDR algorithm. Then the raw GNSS pseudorange, Doppler measurements, and relative motion from PDR are integrated using the FGO. Given the context of pedestrian navigation with a small acceleration most of the time, a novel soft motion model is proposed to smooth the states involved in the factor graph model. The effectiveness of the proposed method is verified step-by-step through two datasets collected in dense urban canyons of Hong Kong using smartphone-level GNSS receivers. The comparison between the conventional extended Kalman filter, several existing methods, and FGO-based integration is presented. The results reveal that the existing FGO-based GNSS standalone positioning is highly complementary to the PDR's relative motion estimation. Both improved positioning accuracy and trajectory smoothness are obtained with the help of the proposed method.**

Index Terms— **GNSS; NLOS; Navigation; Factor graph optimization; Pedestrian dead reckoning; Trajectory smoothing, Urban canyons**

I. INTRODUCTION

The urban canyon is one of the most economic scenarios, posing a significantly increased need for accurate pedestrian navigation [1, 2]. Nowadays, the global navigation satellite system (GNSS) receiver is still one of the most popular sensors in the open area by providing reliable global positioning for users in urban. Unfortunately, the GNSS performs poorly in

urban areas like Hong Kong because of high-rise buildings. The obstacles would lead to the reflection and blockage of the GNSS signals, well-known as the multipath effect and the non-light-of-sight (NLOS) [3]. The multipath effects and NLOS could potentially result in more than tens of meters of error in GNSS positioning. Numerous researchers proposed methods to solve this problem by mitigating the impacts of the multipath effect and NLOS [4-7]. The 3D mapping aided the GNSS positioning method utilized the 3D city model to mitigate the impacts of the potential NLOS and multipath effects, such as the shadow matching algorithms [8, 9]. However, precise 3D building models are required for 3DMA GNSS [8, 9]. Moreover, they relied highly on the accuracy of the initial guess of the user's position which is hard to obtain in deep urban canyons. The recently developed factor graph optimization (FGO) based GNSS positioning methods [10] showed increased resistance against the potential outliers, such as the NLOS and multipath. This is achieved by exploiting measurement redundancy from multiple historical epochs using the factor graph model, where mainly two consecutive epochs of information are exploited simultaneously in the conventional extended Kalman filtering (EKF) based method [11, 12]. The Chemnitz University of Technology team employed the robust model [13-15] to mitigate the effects of outlier measurements in GNSS positioning using the FGO. In their work, only the raw GNSS pseudorange measurements were exploited. As an extension, our recent work in [16] proposed and open-sourced a general FGO-based GNSS positioning framework where both the raw GNSS pseudorange and Doppler measurements are exploited. The result shows that the positioning performance was improved compared to the conventional EKF-based approach from the famous RTKLIB [17]. Interestingly, the recent FGO-based GNSS positioning developed by Dr. Suzuki [18] obtained the best accuracy in the Google Smartphone Challenged in ION GNSS+ 2021 [18] and ION GNSS+ 2022 [19]. His research used switchable constraints [20] together with batch optimization to maintain the trajectory smoothness. The above research showed that the FGO can mitigate the effect of the GNSS outlier by making use of the increased measurement redundancy from historical information. However, the FGO-based GNSS standalone positioning is still challenged in deep urban canyons, resulting in 20 meters of positioning error in highly urbanized areas [16].

Yihan Zhong, Weisong Wen and Li-Ta Hsu, are with Hong Kong Polytechnic University, Hong Kong (correspondence e-mail: welson.wen@polyu.edu.hk)

Inspired by the complementariness between the GNSS and the inertial measurement unit (IMU), the GNSS/IMU integration with the EKF was extensively investigated [21-25]. Similarly, the EKF estimator-based GNSS/ IMU integration can still be sensitive to the outlier measurements. As an extension, the FGO was also utilized to integrate GNSS/IMU navigation system [26-28]. [26] proposed a tightly-coupled GNSS/IMU positioning algorithm based on FGO. [27] investigated the Earth rotation impact regarding positioning accuracy and integrated the refined IMU pre-integration into an FGO-based navigation system to compensate for Earth rotation. [28] proposes an auto regressive integrated moving average (ARIMA) auxiliary model to overcome the GNSS signals interrupt in urban canyons and combine ARIMA and FGO to perform well even equipment outages occur. Although improved performance is obtained, those FGO-based GNSS/INS integration is still limited by the low measurement quality of the smartphone IMU during the occurrence of poor GNSS measurements as the INS-based propagation can quickly diverge without reliable correction from the GNSS. Different from the direct propagating of the raw IMU measurements, the pedestrian dead reckoning (PDR) [29-34] exploits the context of the pedestrian navigation which can provide periodical correction to the IMU by detecting the walking steps. A detailed review of PDR can be found at [35]. Inspired by this, researchers proposed to explore the potential of the GNSS/PDR integration [36-39] via the EKF estimator. For example, the [36] proposed an integrated GNSS/PDR method to bridge the gaps of the GNSS signal outages and combine slide-window, zero crossing, and peak detection methods to detect the occurrence of pedestrian steps. In [37], a real-time Kalman Filter-based GNSS/PDR position method was proposed with a multi-rate filter to prevent GNSS information from being unavailable. The [38] utilizes an EKF-based GNSS/PDR integration to improve the positioning performance of the smartphone-based navigation system in an environment that suffers the multipath effect. However, these EKF-based GNSS/PDR integration fails to explore the measurement redundancy from the historical information, which inspires us to raise a new question: *how would the PDR help with the existing FGO based GNSS positioning as shown in Fig. 1*? Interestingly, the work in [39] investigated a loosely coupled GNSS/PDR integration using the FGO where the position from the GNSS is directly integrated with the PDR. Unfortunately, the high-accuracy Doppler measurement was not exploited and the loosely coupled integration in FGO could not fully exploit the strong time-correlation of the raw GNSS pseudorange measurements [12].

To effectively exploit the complementariness of the recently developed FGO-based GNSS positioning and the PDR, this paper investigates a tightly coupled FGO-based GNSS/PDR integration scheme for smartphone-based pedestrian navigation in urban canyons. On the one hand, the relative motion estimation of PDR can help resist the potential GNSS outliers. On the other hand, the GNSS raw measurements can help to correct the accumulated drift from PDR. More importantly, the global optimization from the FGO is exploited to relax the potential of both positioning sources to obtain an accurate and smooth trajectory which is of great significance for pedestrian navigation applications. Given the context of pedestrian navigation, this paper proposes a smoothness-driven motion

model (SMM) which can effectively capture the dynamics of the pedestrian. The main contributions of this paper are summarized as follows:

(1) As an extension of our previous work in [16, 40], this paper proposes a tightly coupled FGO-based GNSS/PDR integrated positioning method. Specifically, Doppler and pseudorange measurements are tightly-coupled (TC) to connect the state set of two consecutive epochs in the factor graph. The relative motion is derived from the PDR based on the raw measurements from IMU which helps to establish an additional relative connection between the consecutive states.

(2) To effectively capture the dynamics of pedestrian navigation, this paper proposes a smoothness-driven motion model based on the context of pedestrian navigation with a small acceleration for trajectory smoothing which could also help to resist the potential GNSS outliers in GNSS standalone positioning.

(3) This paper verifies the effectiveness of the proposed method step-by-step using the challenging datasets collected in urban canyons of Hong Kong with detailed discussions. Moreover, we compare the proposed FGO-based formulation with the conventional EKF-based methods and several existing methods, again showing the proposed method's effectiveness.
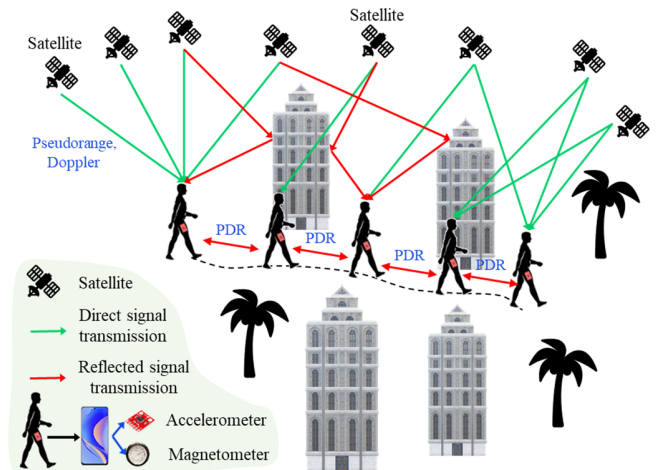

Fig. 1. Illustration of the challenges of the pedestrian navigation in urban canyons with numerous GNSS signal refelctions.

To the best of the author's knowledge, this work is the first research on the tightly-coupled integration of the Doppler and PDR measurements with FGO for a smoother trajectory of pedestrian navigation. The remainder of this paper is organized as follows. An overview of the proposed method is given in Section II. This paper presents the GNSS and PDR integration using FGO in Section III. Two experiments were performed in urban canyons to evaluate the proposed method step by step in Section IV. Discussions are presented in section V. Finally, conclusions and further work are presented in Section VI.

II. OVERVIEW OF THE PROPOSED METHOD

An overview of the proposed method in this paper is shown in Fig. 2. The inputs of the system can be divided into two parts. The first part contains the pseudorange and Doppler measurements from the GNSS receiver in the smartphone. Satellites with a signal-to-noise ratio (SNR) of less than 20 will be excluded. Another part includes the magnetometer and

accelerometer measurements. The output is the state estimation of the smartphone. In the optimization, the GNSS/PDR positioning solution can be obtained by solving the factor graph formulated by the tightly-coupled Doppler factor, the pseudorange factor, the relative motion estimation from PDR, the smoothness-driven motion model, and the constant velocity (CV) factor. The modeling of all the factors above is detailed in Section III.
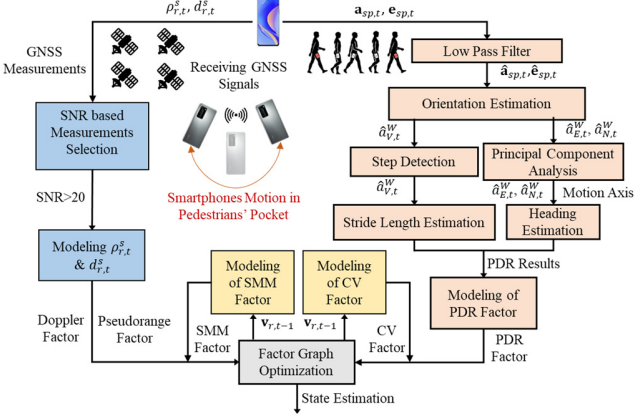

Fig. 2. Overview of the proposed method. The CV denotes the constant velocity model.

Table 1. Symbols and their description in this paper

Symbol	Description
r	The GNSS receiver
s	The index of the satellite
$\rho_{r,t}^s$	The pseudorange measurement received from a satellite s at a given epoch t.
$d_{r,t}^s$	The Doppler measurement received from satellite s at a given epoch t
$\mathbf{p}_t^s$	The position of the satellite s at a given epoch t. $\mathbf{p}_t^s = (p_{t,x}^s, p_{t,y}^s, p_{t,z}^s)^T$
$\mathbf{v}_t^s$	The velocity of the satellite s at a given epoch t. $\mathbf{v}_t^s = (v_{t,x}^s, v_{t,y}^s, v_{t,z}^s)^T$
$\mathbf{p}_{r,t}$	The position of the GNSS receiver at a given epoch t. $\mathbf{p}_{r,t} = (p_{r,t,x}, p_{r,t,y}, p_{r,t,z})^T$
$\mathbf{v}_{r,t}$	The velocity of the GNSS receiver at a given epoch t. $\mathbf{v}_{r,t} = (v_{r,t,x}, v_{r,t,y}, v_{r,t,z})^T$
$\mathbf{a}_{sp,t}$	The raw measurement from the smartphone accelerometers at a given epoch t. $\mathbf{a}_{sp,t} = (a_{sp,t,x}, a_{sp,t,y}, a_{sp,t,z})^T$
$\mathbf{e}_{sp,t}$	The raw measurement from the smartphone magnetometers at a given epoch t. $\mathbf{e}_{sp,t} = (e_{sp,t,x}, e_{sp,t,y}, e_{sp,t,z})^T$
$\hat{\mathbf{a}}_{sp,t}$	The filtered measurement from the accelerometers at a given epoch t in the global coordinate system. $\hat{\mathbf{a}}_{sp,t} = (\hat{a}_{sp,t,x}, \hat{a}_{sp,t,y}, \hat{a}_{sp,t,z})^T$
$\hat{\mathbf{e}}_{sp,t}$	The filtered measurement from the magnetometers at a given epoch t in the global coordinate system. $\hat{\mathbf{e}}_{sp,t} = (\hat{e}_{sp,t,x}, \hat{e}_{sp,t,y}, \hat{e}_{sp,t,z})^T$
$\delta_{r,t}$	The clock bias of the GNSS receiver at a given epoch t
$\delta_{r,t}^s$	The satellite clock bias at a given epoch t

To make the presentation of this paper clear, the notations in Table 1 are defined and are followed by the rest of this paper. Matrices are denoted in uppercase with bold letters. Vectors are denoted in lowercase with bold letters. Variable scalars are denoted as lowercase italic letters. Constant scalars are denoted as lowercase letters. Be noted that the state of the GNSS

receiver and the position of satellites are all expressed in the earth-centered, earth-fixed (ECEF) frame.

III. TIGHTLY COUPLED GNSS/PDR POSITIONING VIA FGO

The proposed factor graph for the GNSS/PDR integrated positioning structure is shown in Fig. 3. The subscript k denotes the total epochs of measurements considered in the FGO. The GNSS receiver state set is represented as follows:

$$\boldsymbol{\chi} = [\mathbf{x}_{r,1}, \mathbf{x}_{r,2}, \ldots, \mathbf{x}_{r,t}, \ldots, \mathbf{x}_{r,k}] \tag{1}$$

$$\mathbf{x}_{r,t} = (\mathbf{p}_{r,t}, \mathbf{v}_{r,t}, \delta_{r,t}, \dot{\delta}_{r,t})^T \tag{2}$$

where the variable $\boldsymbol{\chi}$ denotes the state set of the GNSS receiver ranging from the first epoch to the current k. $\mathbf{x}_{r,t}$ denotes the state of the GNSS receiver at epoch t which involves the position ($\mathbf{p}_{r,t}$), velocity ($\mathbf{v}_{r,t}$, receiver clock bias ($\delta_{r,t}$) and clock drift $\dot{\delta}_{r,t}$.

Each state in the factor graph is connected using a constant velocity model and PDR factors. To smooth the user's trajectories, the SMM factor is also included in our proposed factor graph, which is going to be elaborated in sub-section E. Previously, the formulation of the GNSS pseudorange/loosely-couple Doppler integration using the FGO is first presented in our latest work [16]. For a concise illustration, we briefly present the observation model and error function of pseudorange measurements but an explicit derivation of the Doppler factor which is tightly coupled in the system.
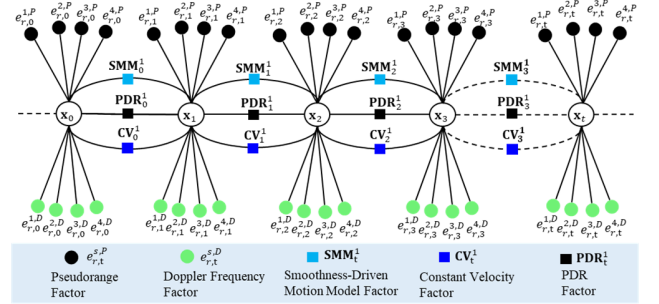

Fig. 3. The factor graph for proposed GNSS/PDR integration..

A. Pseudorange Measurement Modeling

The observation model for GNSS pseudorange measurement from a given satellite s is represented as follows:

$$\rho_{r,t}^s = h_{r,t}^s(\mathbf{p}_{r,t}, \mathbf{p}_t^s, \delta_{r,t}) + \omega_{r,t}^s \tag{3}$$

$$\text{with } h_{r,t}^s(\mathbf{p}_{r,t}, \mathbf{p}_t^s, \delta_{r,t}) = ||\mathbf{p}_t^s - \mathbf{p}_{r,t}|| + \delta_{r,t}$$

where the variable $\omega_{r,t}^s$ stands for the noise associated with the $\rho_{r,t}^s$. Therefore, the error function ($\mathbf{e}_{r,t}^{s,P}$) for a given satellite measurement $\rho_{r,t}^s$ can be represented as follows:

$$||\mathbf{e}_{r,t}^{s,P}||_{\boldsymbol{\Sigma}_{r,t}^s}^2 = ||\rho_{r,t}^s - h_{r,t}^s(\mathbf{p}_{r,t}, \mathbf{p}_t^s, \delta_{r,t})||_{\boldsymbol{\Sigma}_{r,t}^s}^2 \tag{4}$$

where $\boldsymbol{\Sigma}_{r,t}^s$ denotes the covariance matrix. We calculate the $\boldsymbol{\Sigma}_{r,t}^s$ based on the satellite elevation angle (ELE) and SNR following the work in [41].

B. Doppler Measurements Modeling

Given the Doppler measurement $(d_{r,t}^1, d_{r,t}^2, \dots)$ of each satellite at an epoch t. The range rate measurement vector $(\mathbf{y}_{r,t}^d)$ at an epoch t is expressed as follows:

$$\mathbf{y}_{r,t}^d = (\lambda d_{r,t}^1, \lambda d_{r,t}^2, \lambda d_{r,t}^3, \dots)^T \tag{5}$$

where the λ denotes the carrier wavelength of the satellite signal used, the $d_{r,t}^s$ represents the Doppler measurement. The expected range rate $rr_{r,t}^s$ for satellite s can also be calculated as follows:

$$rr_{r,t}^s = \mathbf{e}_{r,t}^{s,LOS}(\mathbf{v}_t^s - \mathbf{v}_{r,t}) + \frac{\omega_{earth}}{c_L}(v_{t,y}^s p_{r,t,x} + p_{t,y}^s v_{r,t,x} - p_{t,x}^s v_{r,t,y} - v_{t,x}^s p_{r,t,y}) + \dot{\delta}_{r,t} \tag{6}$$

where the variable ω_{earth} denotes the angular velocity of the earth's rotation [42]. The variable c_L denotes the speed of light. The variable $\mathbf{e}_{r,t}^{s,LOS}$ denotes the line-of-sight vector connecting the GNSS receiver and the satellite. Furthermore, we can get the error function ($\mathbf{e}_{r,k}^{s,D}$) of the tightly-coupled Doppler measurement as follows:

$$||\mathbf{e}_{r,k}^{s,D}||_{\Sigma_{r,t}^D}^2 = ||\lambda d_{r,t}^s - rr_{r,t}^s||_{\Sigma_{r,t}^D}^2 \tag{7}$$

where $\Sigma_{r,t}^D$ denotes the covariance matrix corresponding to the Doppler measurement. And the $\Sigma_{r,t}^D$ is also calculated based on the ELE and SNR [41] but multiplied by a fixed coefficient valued at 10, which means larger weightings as the Doppler measurements are less sensitive to the GNSS multipath effects.

C. Pedestrian Dead Reckoning Factor Modeling

1) PDR Algorithm

The PDR factor is modeled by following the work in [40]. Only magnetometers and accelerometers are used since the gyroscope is less stable when the smartphone is placed in the pocket of the user's trousers. Both the magnetometer and accelerometer in the smartphone output 3D measurements in local coordinates defined by the smartphone, and the transformation of local coordinates to ECEF frame is necessary for global positioning. The accelerometer measurement $\mathbf{a}_{r,t}$ and the magnetometer measurement $\mathbf{e}_{r,t}$ are first used to determine the orientation of the device. The orientation of the device is estimated in each measurement, and the measured acceleration could be converted to ECEF frame with the Android API *getRotationMatrix* [43], which aims to match the tri-axis acceleration and detected gravity to get the transformation to global coordinate. The three acceleration components are used to determine each step direction and step length. For attenuating the deterioration of dynamic pushes, a low-pass filtering is employed as shown below:

$$\hat{\mathbf{a}}_{sp,t} = (1 - \alpha^{acc})\mathbf{a}_{sp,t} + \alpha^{acc}(\hat{\mathbf{a}}_{sp,t-1}) \tag{8}$$

$$\hat{\mathbf{e}}_{sp,t} = (1 - \alpha^{mag})\mathbf{e}_{sp,t} + \alpha^{mag}(\hat{\mathbf{e}}_{sp,t-1}) \tag{9}$$

where the $\hat{\mathbf{a}}_{sp,i}$ and $\hat{\mathbf{e}}_{sp,i}$ denote the filtered measurements of the accelerometer and magnetometer. α^{acc} and α^{mag} denote the smoothing factor of the corresponding measurement field. Following the previous settings, we empirically set α^{acc} and α^{mag} as 0.6 and 0.84, respectively. The filtered measurements of acceleration can be calculated. The following part will concisely illustrate the detail of the PDR method, including step detection, stride estimation, and heading orientation.

(a) **The step detection**: Under normal pedestrian walking conditions, the vertical acceleration $\hat{a}_{V,t}^W$ reflects a distinct peak and depression for every foot of impact. This feature makes detecting the drop in vertical acceleration as the stride rate feasible. In this paper, we set a dip threshold of 7.5 m/s to avoid a false detection which is experimentally determined.

(b) **The stride length estimation**: We assume that the pedestrian stride is a constant and we can estimate the stride length using the peak-to-peak of vertical acceleration, which was proposed by Weinberg [44], and the model is shown as:

$$l = K_w(a_{V,max} - a_{V,min})^{0.25} \tag{10}$$

where l denotes the estimated stride length, K_w denotes a constant for unit conversion which is empirically set as 0.713. $a_{V,max}$ and $a_{V,min}$ are the maximum and minimum vertical accelerations, respectively.

(c) **Heading direction estimation**: In this paper, the heading direction is estimated in two steps. The first step is to perform a principal component analysis on the 2D plane with $\hat{a}_{E,t}^W$ and $\hat{a}_{N,t}^W$, excluding the vertical direction [30]. After smoothing the two sequences using a moving average, they are subjected to the covariance matrix of Eigenvalue decomposition. The largest eigenvalue result implies the direction estimation in the direction of parallel motion, which is the original forward direction. The second step of the heading direction estimation is to verify whether the original forward direction derived from the PCA is correct. According to [45], vertical and forward accelerations have a time relationship in the same cycle. Usually, the forward acceleration will be followed by a peak immediately after the step detection. By using this property, the forward direction could be decided.

2) PDR Factor

After using the PDR algorithm, we can obtain the relative displacement $\Delta\mathbf{p}_{pdr,t}^{ecef}$ between two consecutive frames under the ECEF coordinate system:

$$\Delta\mathbf{p}_{pdr,t}^{ecef} = [\Delta x_t^{ecef}, \Delta y_t^{ecef}, \Delta z_t^{ecef}] \tag{11}$$

where Δx_t^{ecef}, Δy_t^{ecef} and Δz_t^{ecef} are displacement of the receiver which obtained from the PDR in three different directions. The difference between two consecutive epochs can be represented as:

$$\Delta\mathbf{p}_{r,t} = \mathbf{p}_{r,t} - \mathbf{p}_{r,t-1} \tag{12}$$

Where $\mathbf{p}_{r,t}$ denotes the position of the receiver at the t epoch and the $\mathbf{p}_{r,t-1}$ represents the position of the receiver at the t-1 epoch. Hence, we can get the error function ($\mathbf{e}_{r,t}^R$) for a given relative displacement $\Delta\mathbf{p}_{pdr,t}^{ecef}$ as follows:

$$\left\|\mathbf{e}_{r,t}^R\right\|_{\Sigma_{r,t}^{PDR}}^2 = \left\|\Delta\mathbf{p}_{pdr,t}^{ecef} - \Delta\mathbf{p}_{r,t}\right\|_{\Sigma_{r,t}^{PDR}}^2 \tag{13}$$

where $\Sigma_{r,t}^{PDR}$ denotes the covariance matrix. We set it as the fixed value for denoting the performance of the PDR factor, which is experimentally determined as 0.1.

D. Constant Velocity Factor

The constant velocity factor is constructed based on the assumption that the speed of the pedestrian is nearly invariant in walking. In addition to the velocity remaining constant during walking, the acceleration of the receiver should also converge to zero. Hence, we can get the observation model for the velocity ($\mathbf{v}_{r,t}$) expressed as follows:

$$\mathbf{v}_{r,t} = h_{r,t}^C(\Delta\mathbf{p}_{r,t}, \mathbf{v}_{r,t}, \mathbf{v}_{r,t+1}) + \boldsymbol{\omega}_{r,t}^C \tag{14}$$

$$\text{with } h_{r,t}^C(\Delta\mathbf{p}_{r,t}, \mathbf{v}_{r,t}, \mathbf{v}_{r,t+1}) = \begin{bmatrix} \Delta p_{r,t,x}/\Delta t - (v_{r,t,x} + v_{r,t+1,x})/2 \\ \Delta p_{r,t,y}/\Delta t - (v_{r,t,y} + v_{r,t+1,y})/2 \\ \Delta p_{r,t,z}/\Delta t - (v_{r,t,z} + v_{r,t+1,z})/2 \end{bmatrix},$$

where the $\mathbf{v}_{r,t}$ and $\mathbf{v}_{r,t+1}$ denote the velocity at two consecutive epochs with three-dimension in the ECEF frame, respectively. $\Delta p_{r,t,x}$, $\Delta p_{r,t,y}$, $\Delta p_{r,t,z}$ denote the receiver displacement between the t frame and $t+1$ frame at three dimensions. The variable $\boldsymbol{\omega}_{r,t}^C$ denotes the noise associated with constant motion. Hence, we can get the error function ($\mathbf{e}_{r,t}^C$) for a given receiver velocity measurement $\mathbf{v}_{r,t}$ as follows:

$$||\mathbf{e}_{r,t}^C||_{\Sigma_{r,t}^C}^2 = ||h_{r,t}^C((\Delta\mathbf{p}_{r,t}, \mathbf{v}_{r,t}, \mathbf{v}_{r,t+1}))||_{\Sigma_{r,t}^C}^2 \tag{15}$$

where $\Sigma_{r,t}^C$ denotes the covariance matrix corresponding to the receiver velocity measurement, which is empirically set as fixed value.

E. Smoothness-driven Motion Model Factor

Given the context of pedestrian navigation, the accelerations caused by smartphone motion tend to be small. To exploit this property which can effectively improve the smoothness of the trajectory, this paper proposes a smoothness-driven motion model factor. The acceleration of the GNSS receiver $\mathbf{a}_{r,t}$ can be calculated as follows:

$$\mathbf{a}_{r,t} = \begin{bmatrix} (v_{r,t+1,y} - v_{r,t,y})/\Delta t \\ (v_{r,t+1,y} - v_{r,t,y})/\Delta t \\ (v_{r,t+1,z} - v_{r,t,z})/\Delta t \end{bmatrix} \tag{16}$$

Therefore, we can get the observation model for the acceleration ($\mathbf{a}_{r,t}$) expressed as follows:

$$\mathbf{a}_{r,t} = h_{r,t}^M(0, \mathbf{a}_{r,t}) + \boldsymbol{\omega}_{r,t}^M \tag{17}$$

$$\text{with } h_{r,t}^M(0, \mathbf{a}_{r,t}) = \begin{bmatrix} 0 - (v_{r,t+1,y} - v_{r,t,y})/\Delta t \\ 0 - (v_{r,t+1,y} - v_{r,t,y})/\Delta t \\ 0 - (v_{r,t+1,z} - v_{r,t,z})/\Delta t \end{bmatrix}$$

where the variable $\boldsymbol{\omega}_{r,t}^M$ denotes the noise associated with the zero acceleration model. Hence, we can get the error function ($\mathbf{e}_{r,t}^M$) for a given receiver velocity measurement $\mathbf{v}_{r,t}$ as follows:

$$||\mathbf{e}_{r,t}^M||_{\Sigma_{r,t}^M}^2 = ||\mathbf{a}_{r,t} - h_{r,t}^M(0, \mathbf{a}_{r,t})||_{\Sigma_{r,t}^M}^2 \tag{18}$$

where $\Sigma_{r,t}^M$ denotes the covariance matrix corresponding to the receiver acceleration measurement, which is empirically set as

a fixed value. Based on the factors derived above, the objective function for the GNSS/PDR integration using FGO is formulated as follows:

$$\boldsymbol{\chi}^* = \arg\min_{\boldsymbol{\chi}} \sum_{s,t}(\left|\left|\mathbf{e}_{r,t}^D\right|\right|_{\Sigma_{r,t}^D}^2 + \left|\left|\mathbf{e}_{r,t}^s\right|\right|_{\Sigma_{r,t}^S}^2 + \left|\left|\mathbf{e}_{r,t}^R\right|\right|_{\Sigma_{r,t}^{PDR}}^2 + \left|\left|\mathbf{e}_{r,t}^C\right|\right|_{\Sigma_{r,t}^C}^2 + \left|\left|\mathbf{e}_{r,t}^M\right|\right|_{\Sigma_{r,t}^M}^2) \tag{19}$$

the variable $\boldsymbol{\chi}^*$ denotes the optimal estimation of the state sets, which can be estimated by solving the objective function above. The Ceres Solver [46] is used as a non-linear optimization solver. Meanwhile, the Levenberg-Marquardt (L-M) algorithm [47] is employed in our FGO processes to minimize the cost function iteratively.

IV. EXPERIMENT RESULTS AND DISCUSSION

A. Experiment Setup

Two experimental evaluations are conducted to evaluate the performance of the proposed method. To validate the effectiveness of the proposed FGO-based GNSS/PDR positioning, we collected data in two challenging scenarios (see Figure 4 and Figure 5) with numerous potential multipath effects and NLOS receptions, respectively. During the tests, raw single-frequency GPS and BeiDou measurements were collected at 1 Hz using an Android-based Huawei P40 Pro phone [48]. The same smartphone recorded the accelerometer and magnetometer data via the Android API [48]. In the first experiment, the pedestrian's ground truth is labeled using a high-cost LiDAR/inertial positioning system based on the LIO-SAM [49]. Meanwhile, the loop-closure constraint is used to improve the LiDAR/inertial positioning system's accuracy, which can lead to sub-meter level ground truth positioning. In the second experiment, a highly densely urbanized area with dense traffic, we label the ground truth offline based on Google Earth and the timestamps shown to provide sub-meter accuracy by postprocessing carefully in our previous work [50]. We used an Intel i7-9750K 2.60GHz and a high-performance laptop with 32GB RAM to run the proposed framework.

B. Evaluation Metrics and Methods

The positioning performances are evaluated in the east, north, and up (ENU) frame. Because the GNSS positioning in the vertical direction is highly unreliable due to the satellite geometry in dense urban canyons, in this paper, we only evaluate the horizontal positioning performance, including the root-mean-square of error (RMSE), the mean error (MEAN), standard deviation (STD), maximum error (MAX).

To verify the effectiveness of the proposed method step-by-step, we compared the following methods:

(1) **FGO**: GNSS pseudorange/Doppler integration using FGO [16].

(2) **EKF-PDR**: GNSS pseudorange/Doppler/PDR-based extended Kalman filter.

(3) **FGO-CV**: GNSS pseudorange/tightly-coupled Doppler integration using FGO aided by CV factor.

(4) **FGO-CV-SMM** (1st proposed integration): GNSS pseudorange/tightly-coupled Doppler integration using FGO aided by CV factor and SMM factor.

(5) **FGO-PDR** (2nd proposed integration): GNSS

pseudorange/tightly-coupled Doppler integration using FGO aided by PDR factor.

(6) **FGO-PDR-SMM** (3rd proposed integration): GNSS pseudorange/tightly-coupled Doppler integration using FGO aided by PDR factor and SMM factor.

(7) **FGO-PDR-CV** (4th proposed integration): GNSS pseudorange/tightly-coupled Doppler integration using FGO aided by PDR factor and CV factor.

(8) **FGO-PDR-CV--SMM** (5th proposed integration): GNSS pseudorange/Doppler integration using FGO aided by the PDR, SMM, and CV factor.
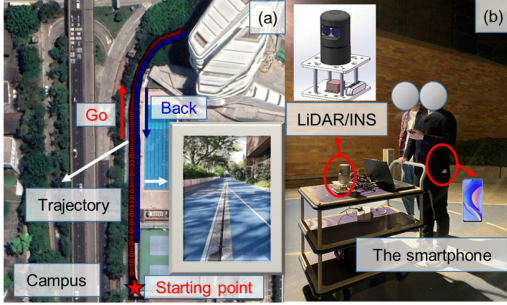
Fig. 4. The scenarios and sensor setup of the campus experiment. (a) the evaluated trajectory during the test. (b) the data collection platform with LiDAR/INS-based ground truth system and smartphone for GNSS data collection.
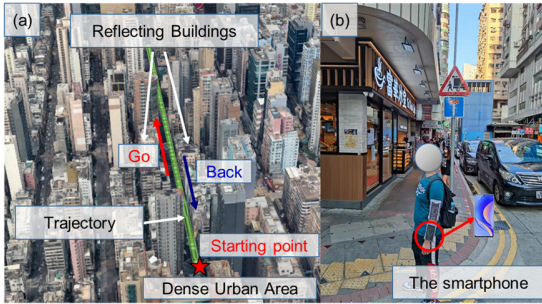

Fig. 5. The sensor setup of the dense urban area. (a) the evaluated trajectory in a dense urban canyon. (b) the data collection platform by hand-hold bag with a smartphone for GNSS data collection.

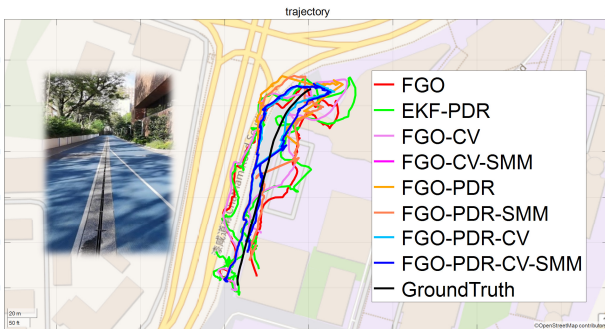## C. Experimental Evaluation on Campus

Fig. 6. 2D positioning trajectories of the evaluated eight methods on the campus. The red curve denotes the trajectory from FGO. The green, light pink, pink, light orange, orange, light blue, and blue colors denote the EKF-PDR, FGO-CV, FGO-CV-SMM, FGO-PDR, FGO-PDR-SMM, FGO-PDR-CV, and FGO-PDR-CV-SMM, respectively.

The 2D positioning trajectories and errors of all the listed positioning methods on the campus are shown in Figure 6 and Figure 7. By comparing the trajectories of all the methods in Figure 6, the trajectory of FGO-PDR-CV-SMM (blue curve) is consistent with the characteristics of pedestrian movement after applying the PDR factor, CV factor, and SMM factor. We can see that the positioning error is significantly reduced near epochs 50 and 150 after adding the PDR factor from Figure 7. Detailed statistic analyses of horizontal errors are shown in Table 2 and Table 3.
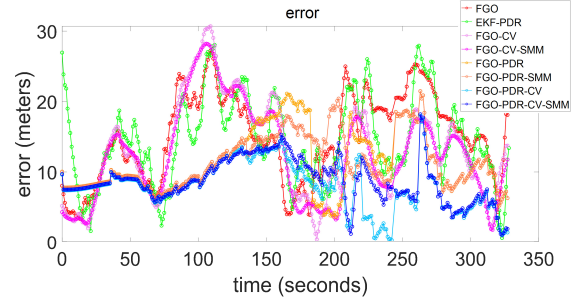

Fig. 7. 2D positioning errors of all the evaluated methods on the campus. The red curve denotes the 2D error from FGO. The green, light pink, pink, light orange, orange, light blue, and blue colors denote the EKF-PDR, FGO-CV, FGO-CV-SMM, FGO-PDR, FGO-PDR-SMM, FGO-PDR-CV, and FGO-PDR-CV-SMM, respectively.

Table 2. Positioning performance of the listed methods in the campus experiment

All Methods	RMSE (m)	MEAN (m)	STD (m)	MAX (m)
FGO	16.17	14.97	6.13	27.23
EKF-PDR	15.80	14.57	6.13	28.05
FGO-CV	14.85	13.13	6.94	30.69
FGO-CV-SMM	14.17	12.53	6.64	28.22
FGO-PDR	12.17	11.32	4.46	21.47
FGO-PDR-SMM	11.99	11.41	3.69	21.48
FGO-PDR-CV	8.63	7.97	3.33	17.98
FGO-PDR-CV-SMM	9.24	8.71	3.07	18.19

Table 3. Horizontal positioning improvements of the listed methods in the campus experiment

Improvements	RMSE (m)	MEAN (m)	STD (m)	MAX (m)
FGO	/	/	/	/
EKF-PDR	2.27%	2.65%	0.07%	-3.02%
FGO-CV	8.19%	12.26%	-13.10%	-12.74%
FGO-CV-SMM	12.36%	16.29%	-8.19%	-3.65%
FGO-PDR	24.77%	24.35%	27.31%	21.16%
FGO-PDR-SMM	25.86%	23.77%	39.82%	21.10%
FGO-PDR-CV	46.61%	46.77%	45.69%	33.95%
FGO-PDR-CV-SMM	42.88%	41.78%	49.94%	33.19%

FGO can achieve 14.97 meters of mean error with 6.13 meters STD. However, the maximum error still reaches 27.23 meters. The mean error decreases to 13.13 meters after applying the TC Doppler factor together with the CV factor (FGO-CV). The improvement shows that the CV factor with TC Doppler can effectively improve positioning performance. However, the CV factor based on pedestrian motion law lacks constraints on acceleration for resisting potential GNSS outliers which would lead to an unsmooth trajectory in GNSS-standalone positioning. After applying our proposed SMM factor, the mean error decreases to 12.53 meters which outperforms FGO-CV.

However, the insufficiency in satellite number and unhealthy GNSS multipath effects would lead to limited improvement.

After applying the PDR to the TC Doppler FGO (FGO-PDR) instead of the CV factor, the mean error decreases to 11.32 meters with a standard deviation of 4.46 meters. This improvement compared with the FGO-CV shows that the PDR factor could provide better relative position constraint between two consecutive epochs. Adding the SMM factor to FGO-PDR could achieve a lower mean of error. However, the improvement is still limited because the PDR factor contains the error source from the smartphone accelerometer and magnetometer which may not obey the pedestrian motion law. After adding the CV factor, the error decreases to 7.97 meters with a significantly reduced standard deviation of 3.33 meters, which shows the effectiveness of the proposed PDR factor. Interestingly, the STD of error could achieve 3.07 meters after applying the SMM factor in FGO-CV-PDR-SMM, but with a larger mean of errors than FGO-CV-PDR. This is due to the occasional non-zero acceleration of the pedestrian during walking in this scenario.
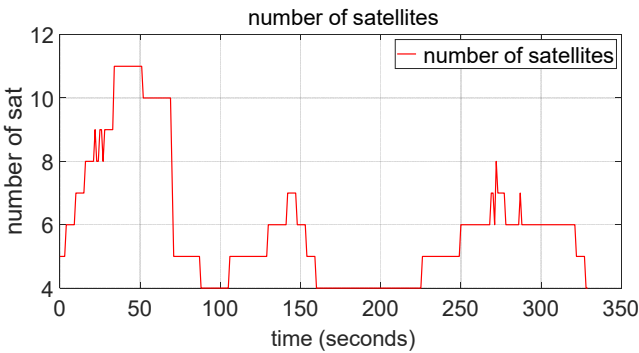

Fig. 8. The relationship between the number of satellites with time.

GNSS/PDR method based on EKF was also evaluated. Its RMSE is 15.80 m, slightly higher than FGO-CV and FGO-CV-SMM. This phenomenon indicates that our tightly-couple GNSS standalone FGO outperforms the EKF-PDR. Figure 8 shows the number of satellites during the experiment. The number of satellites fluctuates during 75 to 150 epochs, which is not ideal for GNSS positioning. We can also see that the errors of FGO-PDR (light orange curve) are significantly smaller than the errors of FGO (red curve) and FGO-CV-SMM (pink curve) during this time which proves that our proposed PDR factor can still play a role in maintaining the need for pedestrian navigation in the GNSS denied environment.

D. Experimental Evaluation in a Dense Urban Area

To challenge the effectiveness of the proposed method for localization in complex scenes, we perform another experiment in a dense urban area. The positioning performances of the above GNSS/PDR integration methods are shown in Table 4 and Table 5. 16.80 meters of mean error is achieved using FGO, which is larger than the one in the campus experiment (14.97 meters) due to the more severe signal reflection caused by denser buildings. After applying the SMM factor, the FGO-CV-

SMM could outperform FGO. This phenomenon confirms that our proposed SMM factor can effectively resist GNSS outliers in dense urban areas. Interestingly, FGO-PDR and FGO-PDR-SMM show similar performance. With the help of the CV factor via FGO-PDR-CV, the error decreases to 13.20 meters with a significantly reduced standard deviation of 6.04 meters, which shows the effectiveness of the assumption of constant velocity in pedestrian navigation. After applying the SMM factor (FGO-PDR-CV-SMM), the mean error can decrease to 13.10 meters, which confirms the SMM factor's effectiveness in resisting potential GNSS outliers in GNSS/PDR integrating positioning in this scenario.

Table 4. Positioning performance of the listed methods in dense urban canyon

All Methods	RMSE (m)	MEAN (m)	STD (m)	MAX (m)
FGO	19.61	16.80	10.11	76.29
EKF-PDR	26.20	21.39	15.15	148.74
FGO-CV	20.53	17.50	10.74	108.94
FGO-CV-SMM	19.42	16.66	9.97	74.02
FGO-PDR	15.12	13.55	6.72	56.92
FGO-PDR-SMM	15.12	13.55	6.72	57.00
FGO-PDR-CV	14.51	13.20	6.04	50.01
FGO-PDR-CV-SMM	14.36	13.10	5.88	45.09

Table 5. Improvements of the listed methods in dense urban canyon

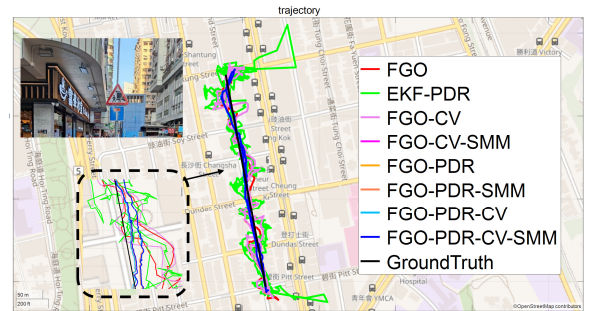| Improvements	RMSE (m)	MEAN (m)	STD (m)	MAX (m)
FGO	/	/	/	/
EKF-PDR	-33.64%	-27.28%	-49.83%	-94.95%
FGO-CV	-4.72%	-4.16%	-6.25%	-42.80%
FGO-CV-SMM	0.96%	0.82%	1.33%	2.98%
FGO-PDR	22.87%	19.35%	33.55%	25.39%
FGO-PDR-SMM	22.87%	19.37%	33.52%	25.29%
FGO-PDR-CV	25.98%	21.46%	40.22%	34.45%
FGO-PDR-CV-SMM	26.78%	22.05%	41.84%	40.91%

Fig. 9. 2D positioning trajectories of the all the evaluated methods in the dense urban area. The red curve denotes the trajectory from FGO. The green, light pink, pink, light orange, orange, light blue and blue colors denote the EKF-PDR, FGO-CV, FGO-CV-SMM, FGO-PDR, FGO-PDR-SMM, FGO-PDR-CV , and FGO-PDR-CV-SMM, respectively.

Figures 9 and 10 show the 2D positioning trajectory and positioning error in the dense urban scenario. In this scenario, the ground truth is a straight line, so we can easily compare the smoothness of all the methods. It is found that the GNSS pseudorange degrades due to signal reflections in dense urban environments would result in outliers that are terrible for the EKF-PDR (green curve). EKF-PDR results are worse than the GNSS-standalone FGO in this scenario, which shows a large error compared to the ground truth. Compared to FGO, FGO-

PDR-CV-SMM shows a significant improvement in terms of the smoothness of the trajectory.
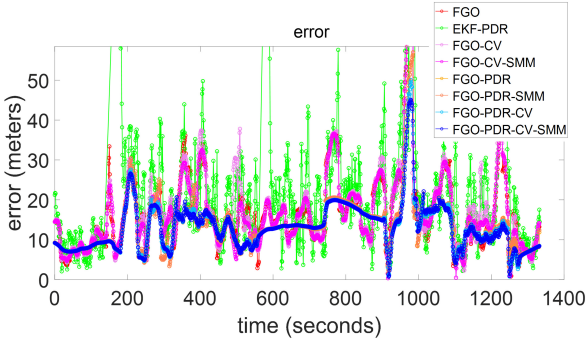

Fig. 10. 2D positioning errors of the evaluated methods in dense urban area. The red curve denotes the 2D error from FGO. The green, light pink, pink, light orange, orange, light blue and blue colors denote the EKF-PDR, FGO-CV, FGO-CV-SMM, FGO-PDR, FGO-PDR-SMM, FGO-PDR-CV, and FGO-PDR-CV-SMM, respectively.

Figure 11 shows the number of satellites during the experiment. FGO-CV (light pink) and FGO-CV-SMM (pink curve), which without adding the PDR factor, reach an error close to 30 meters during epoch 250-400. The FGO-PDR (light orange curve) with the PDR factor added also shows resistance to the decreased data redundancy caused by the insufficient number of satellites.
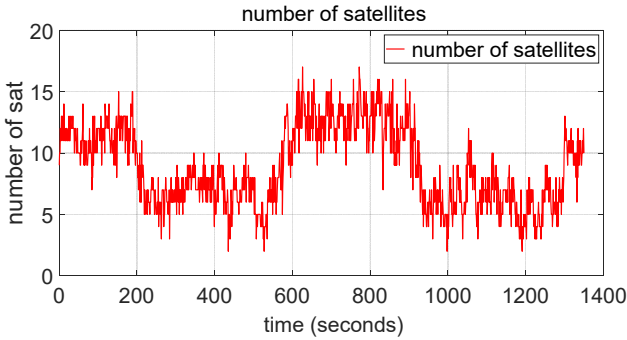

Fig. 11. The relationship between the number of satellites with time.

V. DISCUSSIONS

A. Discussion on PDR Results

Figure 12 shows the performance and trajectory of the PDR algorithm. The PDR algorithm accumulated the errors over time, leading to a significant non-overlap in the positioning results of PDR compared to the ground truth from the trajectory. From Table 6, we can see that the mean value of the positioning error of the PDR localization algorithm in the campus experiment is 21.04 m, while the RMSE is 26.74 m.

Table 6. Performance of the PDR in campus experiment

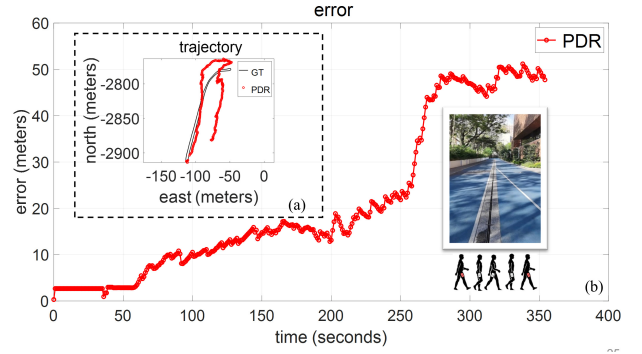| Items	RMSE (m)	MEAN (m)	STD (m)	MAX (m)
PDR	26.74	21.04	16.52	51.18

Fig. 12. (a) 2D positioning trajectory of the PDR in the campus experiment. The black curve denotes the Ground Truth (GT). The red curve denotes the PDR trajectory. (b) 2D positioning error of the PDR in the campus experiment. The red curve denotes the PDR error.
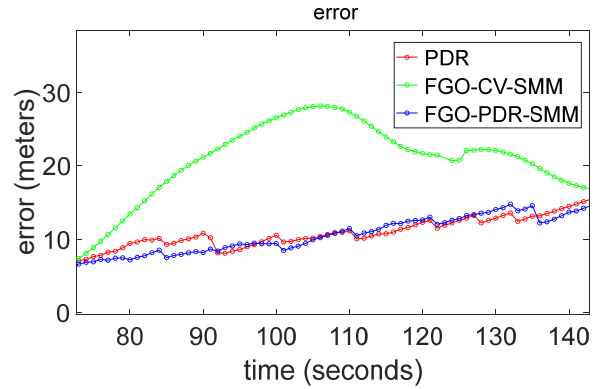

Fig. 13. 2D positioning error of PDR, FGO-CV-SMM, and FGO-PDR-SMM between 70 to 140 epochs in the campus experiment. The red, green, and cyan curves denote PDR, FGO-CV-SMM, and FGO-PDR-SMM, respectively.

Figure 13 shows the error between 70-140 seconds in the campus experiment. During this period, the PDR algorithm has lower errors than the FGO-CV-SMM, indicating that the proposed PDR factor provides better constraints than the CV factor in the estimation process.

B. Discussion on GNSS Measurements Residuals

The performance improvement of FGO-PDR compared to FGO-CV-SMM demonstrate the effectiveness of the PDR factor. Regarding the two pipelines, the investigation of the residuals after the convergence from GNSS measurement models provides insights into the impact of the PDR factor on the derived solution. Ideally, the smaller residuals of applied measurements should potentially lead to more accurate estimation results, as more consistent solution is derived given the assumption that percentage of the healthy measurements exceeds the one from the polluted measurements. Figure 14 shows the histograms comparison of pseudorange and Doppler factor residuals after the optimization using the listed two methods. For the pseudorange measurement, it is shown that the peak of the FGO-CV-SMM pseudorange factor residuals around 0 is higher than the one from the FGO-PDR-CV-SMM. It is well-known that pseudorange is essential for the GNSS standalone positioning because it would offer the absolute position solution. The positioning results of FGO-PDR-CV-SMM can still perform better with larger pseudorange residuals,

compared with the FGO-CV-SMM. One possible reason is that the severe multipath and NLOS phenomenon would significantly degrade the quality of the pseudorange measurements in dense urban areas. As a result, the percentage of the polluted GNSS pseudorange measurements can even exceeds the one from the healthy measurements. This again shows that the GNSS positioning in dense urbna canyons is challenging.
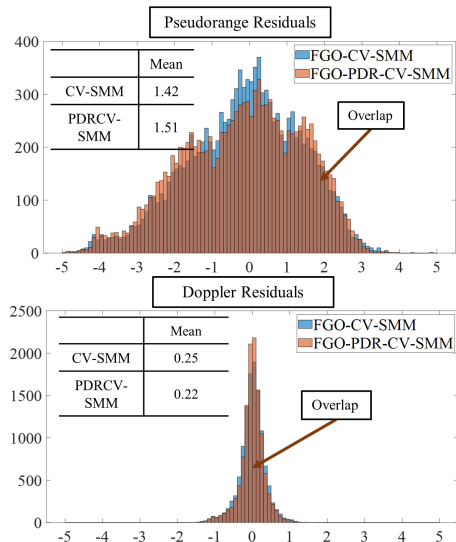

Fig. 14. Histograms of pseudorange factor and Doppler factor residuals. The x-axis denotes the value of residuals. The y-axis denotes the counts of residuals within the histogram.

Interestedly, a different phenomenon occurs in Doppler residuals. The mean value of the FGO-CV-SMM Doppler factor residuals is higher than the mean value FGO-PDR-CV-SMM residuals. The potential reason is that the Doppler is less affected by the multipath effect while the pedestrian is walking along the street [51]. As a result, the assumption that the percentage of healthy measurements exceeds the one from polluted measurements could be largely hold for the Doppler measurements.

VI. CONCLUSIONS AND FUTURE WORK

Pedestrian navigation in urban canyons remains a challenging task. In this paper, we propose an FGO-based GNSS/PDR positioning method that tightly combines information from the GNSS raw measurements and the PDR derived from the magnetometer and accelerometer in the internal inertial measurement unit (IMU) of the smartphone for accurate pedestrian positioning and smoother trajectory estimation. We also verify the effectiveness of the assumption that pedestrians have small acceleration for trajectory smoothing. Applying the SMM factor could help resist the potential GNSS outliers. To effectively capture the dynamics of pedestrian navigation, this paper proposes a smoothness-driven motion model based on the GNSS/PDR localization results based on extended Kalman filtering are also evaluated in this paper, and the method exhibits significant degradation in dense urban canyons due to the influence of GNSS outliers in urban canyons.

In the future, carrier-phase measurements will be added to the FGO-PDR-CV-SMM, which will be used to provide more accurate positioning performance. We will also work on real-time sliding window-based FGO GNSS/PDR positioning to reduce the computational load for real-time applications. We will also exploit collaborative positioning, which could improve measurement redundancy for better positioning performance in the future.

REFERENCES

[1] Y. Li *et al.*, "Toward Location-Enabled IoT (LE-IoT): IoT Positioning Techniques, Error Sources, and Error Mitigation," *IEEE Internet of Things Journal,* vol. 8, no. 6, pp. 4035-4062, 2021, doi: 10.1109/JIOT.2020.3019199.

[2] R. Sun *et al.*, "Improving GPS Code Phase Positioning Accuracy in Urban Environments Using Machine Learning," *IEEE Internet of Things Journal,* vol. 8, no. 8, pp. 7065-7078, 2021, doi: 10.1109/JIOT.2020.3037074.

[3] P. D. Groves, "Principles of GNSS, inertial, and multisensor integrated navigation systems, [Book review]," *IEEE Aerospace and Electronic Systems Magazine,* vol. 30, no. 2, pp. 26-27, 2015.

[4] P. D. Groves, Z. Jiang, M. Rudi, and P. Strode, "A portfolio approach to NLOS and multipath mitigation in dense urban areas," 2013: The Institute of Navigation.

[5] L.-T. Hsu, Y. Gu, and S. Kamijo, "NLOS correction/exclusion for GNSS measurement using RAIM and city building models," *Sensors-Basel,* vol. 15, no. 7, pp. 17329-17349, 2015.

[6] W. W. Wen, G. Zhang, and L.-T. Hsu, "GNSS NLOS exclusion based on dynamic object detection using LiDAR point cloud," *IEEE transactions on intelligent transportation systems,* vol. 22, no. 2, pp. 853-862, 2019.

[7] T. Suzuki and N. Kubo, "Correcting GNSS multipath errors using a 3D surface model and particle filter," in *Proceedings of the 26th International Technical Meeting of the Satellite Division of The Institute of Navigation (ION GNSS+ 2013)*, 2013, pp. 1583-1595.

[8] P. Groves, "It's time for 3D mapping–aided GNSS," *Inside GNSS Magazine,* pp. 50-56, 2016.

[9] Y. Wada, L.-T. Hsu, Y. Gu, and S. Kamijo, "Optimization of 3D building models by GPS measurements," *GPS Solutions,* vol. 21, no. 1, pp. 65-78, 2017/01/01 2017, doi: 10.1007/s10291-015-0504-y.

[10] N. Sünderhauf and P. Protzel, "Towards robust graphical models for GNSS-based localization in urban environments," in *International Multi-Conference on Systems, Signals & Devices*, 2012: IEEE, pp. 1-6.

[11] T. D. Barfoot, *State estimation for robotics*. Cambridge University Press, 2017.

[12] W. Wen, T. Pfeifer, X. Bai, and L.-T. Hsu, "Factor graph optimization for GNSS/INS integration: A comparison with the extended Kalman filter,"

NAVIGATION: Journal of the Institute of Navigation, vol. 68, no. 2, pp. 315-331, 2021.

[13] T. Pfeifer and P. Protzel, "Expectation-maximization for adaptive mixture models in graph optimization," in *2019 International Conference on Robotics and Automation (ICRA)*, 2019: IEEE, pp. 3151-3157.

[14] T. Pfeifer and P. Protzel, "Robust sensor fusion with self-tuning mixture models," in *2018 IEEE/RSJ International Conference on Intelligent Robots and Systems (IROS)*, 2018: IEEE, pp. 3678-3685.

[15] T. Pfeifer, S. Lange, and P. Protzel, "Dynamic Covariance Estimation—A parameter free approach to robust Sensor Fusion," in *2017 IEEE International Conference on Multisensor Fusion and Integration for Intelligent Systems (MFI)*, 2017: IEEE, pp. 359-365.

[16] W. Wen and L.-T. Hsu, "Towards robust GNSS positioning and Real-time kinematic using factor graph optimization," in *2021 IEEE International Conference on Robotics and Automation (ICRA)*, 2021: IEEE, pp. 5884-5890.

[17] T. Takasu and A. Yasuda, "Development of the low-cost RTK-GPS receiver with an open source program package RTKLIB," in *International symposium on GPS/GNSS*, 2009, vol. 1: International Convention Center Jeju Korea.

[18] T. Suzuki, "First place award winner of the smartphone decimeter challenge: global optimization of position and velocity by factor graph optimization," in *Proceedings of the 34th International Technical Meeting of the Satellite Division of The Institute of Navigation (ION GNSS+ 2021)*, 2021, pp. 2974-2985.

[19] T. Suzuki, "1st Place Winner of the Smartphone Decimeter Challenge: Two-Step Optimization of Velocity and Position Using Smartphone's Carrier Phase Observations," in *Proceedings of the 35th International Technical Meeting of the Satellite Division of The Institute of Navigation (ION GNSS+ 2022)*, 2022, pp. 2276-2286.

[20] N. Sünderhauf and P. Protzel, "Switchable constraints for robust pose graph SLAM," in *2012 IEEE/RSJ International Conference on Intelligent Robots and Systems*, 2012: IEEE, pp. 1879-1884.

[21] G. Falco, M. Pini, and G. Marucco, "Loose and tight GNSS/INS integrations: Comparison of performance assessed in real urban scenarios," *Sensors,* vol. 17, no. 2, p. 255, 2017.

[22] G. Falco, M. Campo-Cossío, and A. Puras, "MULTI-GNSS receivers/IMU system aimed at the design of a heading-constrained Tightly-Coupled algorithm," in *2013 International Conference on Localization and GNSS (ICL-GNSS)*, 25-27 June 2013 2013, pp. 1-6, doi: 10.1109/ICL-GNSS.2013.6577263.

[23] K.-W. Chiang, T. T. Duong, and J.-K. Liao, "The Performance Analysis of a Real-Time Integrated INS/GPS Vehicle Navigation System with Abnormal GPS Measurement Elimination," *Sensors,* vol. 13, no. 8, pp. 10599-10622, 2013. [Online]. Available: https://www.mdpi.com/1424-8220/13/8/10599.

[24] G. Gao and G. Lachapelle, "A novel architecture for ultra-tight HSGPS-INS integration," *Positioning,* vol. 1, no. 13, 2008.

[25] Q. Zhang, X. Niu, and C. Shi, "Impact assessment of various IMU error sources on the relative accuracy of the GNSS/INS systems," *IEEE Sensors Journal,* vol. 20, no. 9, pp. 5026-5038, 2020.

[26] W. Li, X. Cui, and M. Lu, "A robust graph optimization realization of tightly coupled GNSS/INS integrated navigation system for urban vehicles," *Tsinghua Science and Technology,* vol. 23, no. 6, pp. 724-732, 2018, doi: 10.26599/TST.2018.9010078.

[27] H. Tang, T. Zhang, X. Niu, J. Fan, and J. Liu, "Impact of the Earth Rotation Compensation on MEMS-IMU Preintegration of Factor Graph Optimization," *IEEE Sensors Journal,* vol. 22, no. 17, pp. 17194-17204, 2022, doi: 10.1109/JSEN.2022.3192552.

[28] Q. Li, L. Zhang, and X. Wang, "Loosely Coupled GNSS/INS Integration Based on Factor Graph and Aided by ARIMA Model," *IEEE Sensors Journal,* vol. 21, no. 21, pp. 24379-24387, 2021, doi: 10.1109/JSEN.2021.3112490.

[29] S. Beauregard and H. Haas, "Pedestrian dead reckoning: A basis for personal positioning," in *Proceedings of the 3rd Workshop on Positioning, Navigation and Communication*, 2006, pp. 27-35.

[30] U. Steinhoff and B. Schiele, "Dead reckoning from the pocket-an experimental study," in *2010 IEEE international conference on pervasive computing and communications (PerCom)*, 2010: IEEE, pp. 162-170.

[31] Q. Wang *et al.*, "Pedestrian Dead Reckoning Based on Walking Pattern Recognition and Online Magnetic Fingerprint Trajectory Calibration," *IEEE Internet of Things Journal,* vol. 8, no. 3, pp. 2011-2026, 2021, doi: 10.1109/JIOT.2020.3016146.

[32] D. Yan, C. Shi, T. Li, and Y. Li, "FlexPDR: Fully Flexible Pedestrian Dead Reckoning Using Online Multimode Recognition and Time-Series Decomposition," *IEEE Internet of Things Journal,* vol. 9, no. 16, pp. 15240-15254, 2022, doi: 10.1109/JIOT.2022.3147473.

[33] C. Chen, P. Zhao, C. X. Lu, W. Wang, A. Markham, and N. Trigoni, "Deep-Learning-Based Pedestrian Inertial Navigation: Methods, Data Set, and On-Device Inference," *IEEE Internet of Things Journal,* vol. 7, no. 5, pp. 4431-4441, 2020, doi: 10.1109/JIOT.2020.2966773.

[34] W. Chen, R. Chen, Y. Chen, H. Kuusniemi, and J. Wang, "An effective Pedestrian Dead Reckoning algorithm using a unified heading error model," in *IEEE/ION Position, Location and Navigation Symposium*, 4-6 May 2010 2010, pp. 340-347, doi: 10.1109/PLANS.2010.5507300.

[35] R. Harle, "A survey of indoor inertial positioning systems for pedestrians," *IEEE Communications Surveys & Tutorials,* vol. 15, no. 3, pp. 1281-1293, 2013.

[36] C. Wei *et al.*, "An integrated GPS and multi-sensor pedestrian positioning system for 3D urban navigation," in *2009 Joint Urban Remote Sensing*

Event, 20-22 May 2009 2009, pp. 1-6, doi: 10.1109/URS.2009.5137690.

[37] M. Basso, A. Martinelli, S. Morosi, and F. Sera, "A Real-Time GNSS/PDR Navigation System for Mobile Devices," *Remote Sensing,* vol. 13, no. 8, p. 1567, 2021. [Online]. Available: https://www.mdpi.com/2072-4292/13/8/1567.

[38] A. Rehman, H. Shahid, M. A. Afzal, and H. M. A. Bhatti, "Accurate and Direct GNSS/PDR Integration Using Extended Kalman Filter for Pedestrian Smartphone Navigation," *Gyroscopy and Navigation,* vol. 11, no. 2, pp. 124-137, 2020/04/01 2020, doi: 10.1134/S2075108720020054.

[39] C. Jiang *et al.*, "Smartphone PDR/GNSS Integration via Factor Graph Optimization for Pedestrian Navigation," *IEEE Transactions on Instrumentation and Measurement,* vol. 71, pp. 1-12, 2022.

[40] L.-T. Hsu, Y. Gu, Y. Huang, and S. Kamijo, "Urban pedestrian navigation using smartphone-based dead reckoning and 3-D map-aided GNSS," *IEEE Sensors Journal,* vol. 16, no. 5, pp. 1281-1293, 2015.

[41] A. M. Herrera, H. F. Suhandri, E. Realini, M. Reguzzoni, and M. C. de Lacy, "goGPS: open-source MATLAB software," *Gps Solut,* vol. 20, no. 3, pp. 595-603, 2016.

[42] T. Takasu and A. Yasuda, "Development of the low-cost RTK-GPS receiver with an open source program package RTKLIB," in *International symposium on GPS/GNSS*, 2009: International Convention Center Jeju Korea, pp. 4-6.

[43] S. Malkos, "Google to Provide Raw GNSS Measurements: User Location Takes Center Stage in New Android OS," *GPS World,* vol. 27, no. 7, p. 36, 2016.

[44] H. Weinberg, "Using the ADXL202 in pedometer and personal navigation applications," *Analog Devices AN-602 application note,* vol. 2, no. 2, pp. 1-6, 2002.

[45] D. Kamisaka, S. Muramatsu, T. Iwamoto, and H. Yokoyama, "Design and implementation of pedestrian dead reckoning system on a mobile phone," *IEICE transactions on information and systems,* vol. 94, no. 6, pp. 1137-1146, 2011.

[46] S. Agarwal and K. Mierle, "Ceres solver," 2012.

[47] J. J. Moré, "The Levenberg-Marquardt algorithm: implementation and theory," in *Numerical analysis*: Springer, 1978, pp. 105-116.

[48] T. Wübbena, F. Darugna, A. Ito, and J. Wübbena, "Geo++'s Experiments on Android GNSS Raw Data," in *Proceedings of the GNSS Raw Measurements Taskforce Workshop, GSA Headquarters*, 2018.

[49] T. Shan, B. Englot, D. Meyers, W. Wang, C. Ratti, and D. Rus, "Lio-sam: Tightly-coupled lidar inertial odometry via smoothing and mapping," in *2020 IEEE/RSJ international conference on intelligent robots and systems (IROS)*, 2020: IEEE, pp. 5135-5142.

[50] H.-F. Ng, G. Zhang, and L.-T. Hsu, "A computation effective range-based 3D mapping aided GNSS with NLOS correction method," *The Journal of Navigation,* vol. 73, no. 6, pp. 1202-1222, 2020.

[51] P. Xie and M. G. Petovello, "Measuring GNSS multipath distributions in urban canyon environments," *IEEE Transactions on Instrumentation and Measurement,* vol. 64, no. 2, pp. 366-377, 2014.

Yihan Zhong Yihan Zhong obtained his bachelor's degree in process equipment and control engineering from Guangxi University in 2020 and a Master's degree from The Hong Kong Polytechnic University (PolyU). He is currently a Ph.D. student at the Department of Aeronautical and Aviation Engineering (AAE) of PolyU. His research interests include factor graph optimization-based collaborative positioning and low-cost localization.
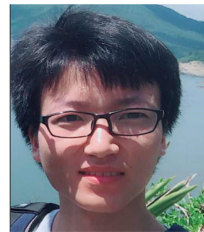
Weisong Wen was born in Ganzhou, Jiangxi, China. He received a Ph.D. degree in mechanical engineering, the Hong Kong Polytechnic University. He was a visiting student researcher at the University of California, Berkeley (UCB) in 2018. He is currently a research assistant professor in the Department of Aeronautical and Aviation Engineering. His research interests include multi-sensor integrated localization for autonomous vehicles, SLAM, and GNSS positioning in urban canyons.

Li-Ta Hsu received the B.S. and Ph.D. degrees in aeronautics and astronautics from National Cheng Kung University, Taiwan, in 2007 and 2013, respectively. He is currently an assistant professor with the Department of Aeronautical and Aviation Engineering. The Hong Kong Polytechnic University, before he served as a post-doctoral researcher in the Institute of Industrial Science at the University of Tokyo, Japan. In 2012, he was a visiting scholar at University College London, the U.K. His research interests include GNSS positioning in challenging environments and localization for pedestrian, autonomous driving vehicle, and unmanned aerial vehicle.